






Optical mode enabled manipulation of topological phase in waveguide-based scattering networksChangyu Zhou ¹, Zhenwei Xie,^{1,*} Ting Lei ¹, Yao Zhang ², Qinmiao Chen,² and Xiaocong Yuan ^{1,†}¹*Nanophotonics Research Center, Institute of Microscale Optoelectronics & State Key Laboratory of Radio Frequency Heterogeneous Integration, Shenzhen University, Shenzhen 518060, China*²*State Key Laboratory on Tunable Laser Technology, Ministry of Industry and Information Technology Key Lab of Micro-Nano Optoelectronic Information System, Harbin Institute of Technology (Shenzhen), Shenzhen 518055, China* (Received 19 October 2023; revised 9 July 2024; accepted 25 July 2024; published 19 August 2024)

In a topological system with an edge, the number of edge states is typically determined by the bulk topological invariant, as per the well-established bulk-boundary correspondence. However, anomalous topological edge states can arise in periodically driven Floquet systems even when the bulk Chern number is zero. A topological invariant (winding number) has been introduced to establish the appropriate bulk-boundary correspondence in such systems. Nevertheless, manipulating the topological properties of systems, whether static or driven, remains a significant challenge. In photonic systems, optical fields with diverse inherent dimensions such as frequency and polarization offer a natural avenue for topological-phase manipulation. In this paper, we present an alternative scheme for switching the topological invariant (winding number) of the system by changing the optical-waveguide mode within an integrated waveguide-based scattering network. With creating a bonding interface, this topological-phase switching facilitates the transmissions of the interface state in different directions. Experimental validation of this concept is demonstrated using a ring-optical-waveguide device. In this paper, we introduce an alternative strategy for tailoring the topological properties of optical systems.

DOI: [10.1103/PhysRevB.110.075424](https://doi.org/10.1103/PhysRevB.110.075424)**I. INTRODUCTION**

Topological edge states convey a crucial message about the topological characteristics of diverse physical systems. In a two-dimensional gapped system, there must exist edge states that are localized at the interface of two topologically nonequivalent materials, with energies falling within the gap. According to the bulk-boundary correspondence [1–3], the number of these states is determined by the topological invariants in the surrounding systems, namely, the Chern number, which characterizes the topological property of the wave functions throughout the Brillouin zone. Notably, Chern number remains constant unless the energy gap is closed somewhere, rendering the edge states robust against certain disorders if the topological properties of the systems remain unchanged [4].

The scenario is somewhat different for periodically driven systems, also known as Floquet systems, in which the phase spectrum (i.e., the quasienergy band) is periodic and unbounded [5,6]. Edge states can still arise in a system with a vanishing Chern number, challenging the conventional bulk-boundary correspondence. Rudner *et al.* [6] introduced an alternative topological invariant, the winding number, through which a more adaptable bulk-boundary correspondence was established for periodically driven systems. This approach reveals that the existence of anomalous edge states can be fully characterized by the winding number of each Floquet gap. Subsequently, these anomalous edge states were

observed and validated in photonic systems [7–10]. In parallel to the tight-binding description for Floquet systems, the scattering-network scheme [11–13], proposed by Chalker and Coddington [14] for studying quantum Hall systems, is an alternative method to describe such systems. Authors of recent studies have demonstrated that edge-state transmission in scattering networks can withstand strong disordered and amorphous perturbations [15,16], protecting the systems against fabrication imperfections. In addition, photonic topological systems have paved a path for simulating band topology [17,18]. One of the powerful platforms is the microring-waveguide-based configuration, which has been introduced to study various topological systems [19–22] and the scattering-network models [23–25], showcasing promising potential for diverse applications in photonics [26–28].

It is noteworthy that the topological phase for these photonic systems can be manipulated by leveraging frequency [9,15,16] and polarization [29,30] degrees of freedom (DOFs). However, the manipulations involve the trivial bulk states, rendering them unsuitable for photonic applications. In addition, frequency manipulation stands out as a natural choice due to the frequency dispersion in photonic systems and its ease of implementation with tailored systems, leaving other DOFs largely untapped. In this paper, we present an alternative approach that enables the manipulation of a topological invariant by the switching between optical-waveguide transverse electric (TE) and transverse magnetic (TM) modes in a ring-optical-waveguide (ROW)-based scattering-network system. Through constructing a bonding interface, the generated anomalous interface state transitions to an alternate direction upon mode alteration. As a proof of concept, we

*Contact author: ayst31415926@szu.edu.cn†Contact author: xcyuan@szu.edu.cn

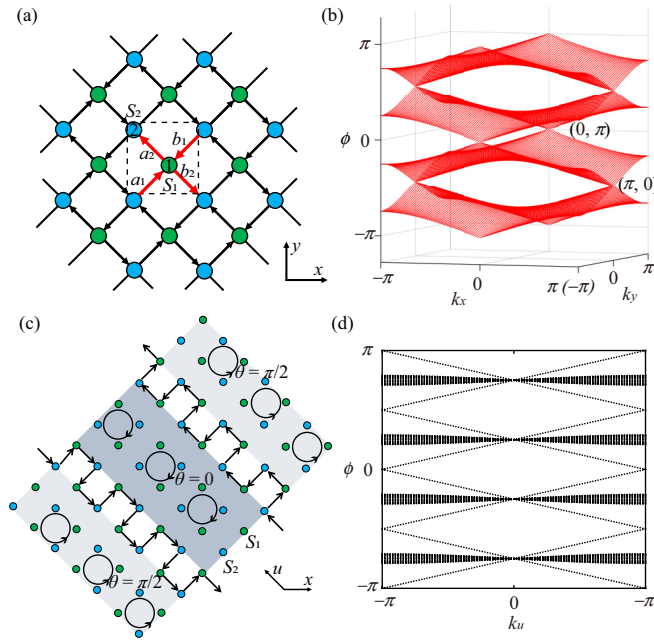


FIG. 1. Analysis of the scattering-network model. (a) The square network with a dashed-line marked unit cell. Each unit cell contains two inequivalent scattering elements (S_1, S_2) and four inequivalent links (a_1, b_1, a_2, b_2). (b) The phase spectrum (quasienergy band) of the Ho-Chalker evolution operator of the network model at criticality $\theta = \pi/4$. (c) Emergence of the interface state (marked by the black arrows) at an interface between the two phases $\theta = \pi/2$ and 0 . The propagating direction is dependent on the bonding sequence of the adjacent phases. (d) Eigenvalue phase spectrum of the Ho-Chalker evolution operator for lattice with an infinite cylindrical strip geometry, which involves the $\theta \approx \pi/2$ and 0 phases with two interfaces. Here, k_u is the quasimomentum in the direction parallel to the interface of the cylinder, as shown in (c).

$$S(\theta, \mathbf{k}) = \begin{bmatrix} 0 & 0 & \cos \theta \exp(-ik_y) & i \sin \theta \exp(-ik_x) \\ 0 & 0 & i \sin \theta \exp(ik_x) & \cos \theta \exp(ik_y) \\ \sin \theta & i \cos \theta & 0 & 0 \\ i \cos \theta & \sin \theta & 0 & 0 \end{bmatrix}, \quad (2)$$

and the state basis is $\psi = [a_1(\mathbf{k}), b_1(\mathbf{k}), a_2(\mathbf{k}), b_2(\mathbf{k})]^T$. The quasienergy spectrum ϕ of $S(\theta, \mathbf{k})$ reveals that the bands intersect at the Dirac points $\mathbf{k} = (\pi, 0)$ and $(0, \pi)$ at $\theta = \pi/4$ [Fig. 1(b)]. As θ deviates from $\pi/4$, these Dirac points transition into band gaps with positive and negative mass separately, eventually giving rise to four flat bands at $\theta = 0$ or $\pi/2$. A conceptual explanation is that each band possesses both positive and negative Berry flux, resulting in a vanishing Chern number for all θ [32].

Remarkably, even though both the phases of $\theta > \pi/4$ and $\theta < \pi/4$ have zero Chern numbers, an edge state can still appear at their interface. The bulk winding number W_η for each gap $\eta = -\pi/2 + m\pi/2$ ($m = 0, 1, 2, 3$) in the quasienergy spectrum serves to distinguish these two distinct phases of the network. According to Ref. [12], the calculated winding number $W_{\eta=0} (= W_{\eta=\pi})$ is equal to 1 for the $\theta < \pi/4$ phase

experimentally demonstrate this switching of the anomalous interface state by changing the waveguide mode within a ROW-network device. This methodology offers a promising alternative for manipulating the topological properties of physical systems.

II. THEORETICAL ANALYSIS

The proposed network model comprises a series of paired ROWs arrayed periodically in both x and y directions. The selected ROW-based network system can be equivalent to a square Bravais lattice, where each unit cell consists of two nonequivalent scattering elements (S_1, S_2) and four distinct links (a_1, b_1, a_2, b_2). The inputs are denoted by (a_1, b_1) and the outputs by (a_2, b_2) of a ROW within the network [see Fig. 1(a)]. The unitary matrix S_μ ($\mu = 1, 2$) characterizes the scattering between the links and can be parametrized by

$$S_\mu = \begin{pmatrix} \cos \theta_\mu & i \sin \theta_\mu \\ i \sin \theta_\mu & \cos \theta_\mu \end{pmatrix}, \quad (1)$$

where θ_μ controls the transmission and reflection during the scattering process. For simplicity, we adopt $\theta_2 = \pi/2 - \theta_1 = \theta$ in this paper.

One approach for studying the topology of a network model involves employing the Floquet operator formalism, a well-documented method in the literature [5,6]. However, analyzing all the distributed edge states using this method can be intricate in our design. Instead, we have opted to utilize the Ho-Chalker evolution operator, which encompasses different scattering processes simultaneously [12,31]. By considering the analysis in momentum space and introducing the quasi-momentum $\mathbf{k} = (k_x, k_y)$, the Bloch version of the Ho-Chalker operator for the unit cell in Fig. 1(a) is presented as [12]

and 0 for the $\theta > \pi/4$ phase. Similarly, $W_{\eta=\pi/2} (= W_{\eta=-\pi/2})$ is also equal to 1 for the $\theta < \pi/4$ phase and 0 for the $\theta > \pi/4$ phase. This indicates that the $\theta < \pi/4$ and $\theta > \pi/4$ phases are topologically inequivalent. Although the value of W_η relies on the chosen unit cell, the difference $W_\eta[\theta < \pi/4] - W_\eta[\theta > \pi/4]$ is an invariant that accurately reflects the number of anomalous states at the interface between these phases. As shown in Figs. 1(c) and 1(d), a propagating state is located at the interface between these two phases ($\theta = \pi/2$ and 0), with its propagating direction contingent on the bonding sequence of the two phases. Moreover, by adjusting the parameter θ , the topological phase of the network can be manipulated to govern the propagation direction of the interface state. This means that the topology of the system can be altered by adjusting the parameter θ , as elucidated in the preceding analysis.

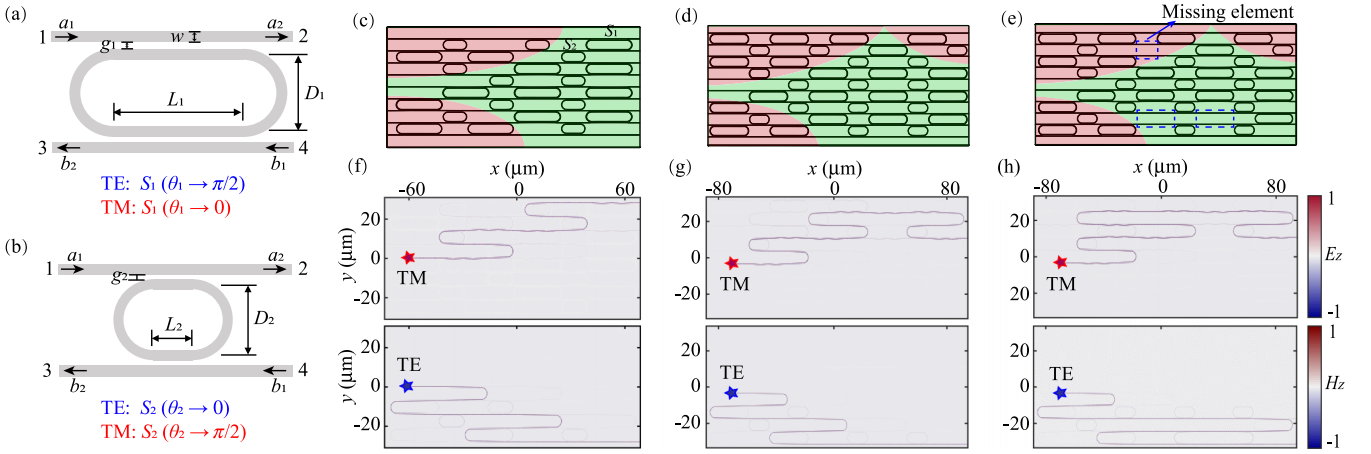


FIG. 2. Simulation results of the topological interface state. Schematic illustrations for ring optical-waveguides (ROWS) (a) S_1 and (b) S_2 in the network. Each of them has two inputs (a_1, b_1) and two outputs (a_2, b_2). Schematic illustrations of the ROWs-network designs for (c) normal, (d) L-type deflected, and (e) defective-interfaces configurations. The used ROWs S_1 and S_2 are marked in (c), and the red and green shaded regions represent two different domains ($\theta \approx 0$ and $\pi/2$ phases). Simulated field distributions for (f) normal, (g) L-type deflected, and (h) defective-interfaces configurations. The input transverse magnetic (TM) and transverse electric (TE) modes are marked by the red and blue star, respectively. All the results are simulated at the wavelength of 1552 nm.

III. SIMULATION RESULTS

Significantly, the parameter θ , which determines the input and output amplitudes of a single ROW, can be adjusted by changing the mode in the waveguide while keeping the network model unchanged. This provides an opportunity to manipulate the topology of the system. As an example, we have designed two silicon ROWs to simulate the scattering elements S_1 and S_2 . Each ROW consists of a segments-embedded ring waveguide and two side-coupled straight waveguides [Figs. 2(a) and 2(b)], and the coupling between drop- and through-waveguide channels can be parameterized by θ , as shown in Eq. (1). The silicon waveguides in our design have a width of $w = 420$ nm and a height of $h = 350$ nm, allowing only the fundamental TE_0 and TM_0 modes. Other designed parameters include the gap distance g_μ between the straight and ring waveguides, the length L_μ of the embedded segments in the ring waveguide, and the diameter D_μ of the ring waveguide. In our design, these parameters are $g_1 = 0.1 \mu\text{m}$, $L_1 = 20.5 \mu\text{m}$, and $D_1 = 6 \mu\text{m}$ for the ROW of S_1 [Fig. 2(a)] and $g_2 = 0.16 \mu\text{m}$, $L_2 = 8 \mu\text{m}$, and $D_2 = 5.88 \mu\text{m}$ for the ROW of S_2 [Fig. 2(b)]. These two ROWs are designed to transmit or reflect the TE (TM) mode as much as possible, with the effective parameters $\theta_1 \approx \pi/2$ and $\theta_2 \approx 0$ for the waveguide TE mode, and $\theta_1 \approx 0$ and $\theta_2 \approx \pi/2$ for the TM mode. These configurations simulate the switching of the parameters θ_1 and θ_2 in the scattering network (see Appendix C for design details). In this setup, the bulk topology can be accurately controlled by simply changing the mode of the input optical field. It should be noted that this process assumes a lossless scenario [see Eq. (1)]. However, in actual ROWs, some loss is inevitable, leading to lower efficiency and spectrum deviation in the response of the ROWs. Nevertheless, the designed ROWs are intended to operate in the off-resonance range (Appendix C), minimizing the influence on the system parameter θ_μ .

Upon analysis, it is noteworthy that the state localized at the bonding interface between two topologically inequivalent phases will move toward the opposite direction when the mode switches. To demonstrate this concept, we constructed a single network-model device that incorporates two interfaces formed by bonding the two topologically inequivalent phases $\theta \approx 0$ and $\pi/2$ in both ordered and antioordered manners, as shown in Figs. 2(c)–2(e). With this approach, the state at each interface can be quantitatively analyzed separately. The designed two interfaces on the device can be regarded as two channels in response to the waveguide TE and TM modes separately. Each channel is allowed to transmit one mode while suppressing the other one under specific wavelengths. Figure 2(f) shows the simulation results of the field distributions in this ROW-based system. When the device is excited with a TM mode, light is guided at one interface and eventually exits from the upper waveguide. Conversely, for the excited TE mode, light is guided along the other interface and exits from the lower waveguide. Additionally, we have designed an L-type deflected interface [Fig. 2(d)] and the defective interfaces that lack some scattering elements [Fig. 2(e)], and the simulation results are depicted in Figs. 2(g) and 2(h), respectively. These results demonstrate that the interface state remains unaffected by the deflection or defective perturbation if the topological properties of surrounding systems remain unchanged.

Figure 3 illustrates the simulated efficiency curves for the three configurations designed in Figs. 2(c)–2(e). At specific wavelengths (indicated by gray shaded regions), the transmission of the TM mode is predominant in the TM-interface channel, while the TE-mode transmission prevails in the TE-interface channel. For instance, considering the results at a wavelength of 1552 nm, in the TM-interface channel, the simulation efficiencies of the TM mode for the three configurations are approximately -1.3 dB (74%), -1.8 dB (66%), and -1.3 dB (74%) [Figs. 3(a)–3(c)], respectively. The

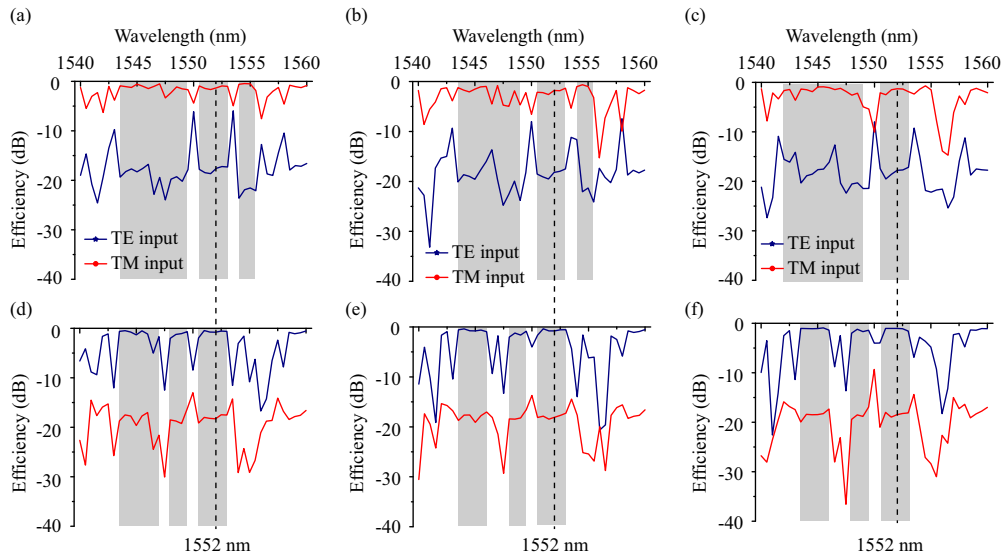


FIG. 3. Simulated efficiency curves for characterizing the topological interface state. Simulated efficiency curves in the transverse magnetic (TM) interface channel for three types of configurations: (a) normal, (b) L-type deflected, and (c) defective interfaces. The gray shaded regions indicate the range of well-working wavelengths. The blue and red curves represent the tested results for transverse electric (TE) and TM modes, respectively. Simulated efficiency curves in the TE interface channel for (d) normal, (e) L-type deflected, and (f) defective-interfaces configurations.

corresponding mode-extinction ratios, calculated by the logarithm of the ratio between the desired and undesired modes, are ~ 16.3 , 16.4 , and 16.5 dB, respectively. In contrast, in the TE-interface channel, the simulation efficiencies of the TE mode for the corresponding three configurations are approximately -0.8 dB (83%), -0.8 dB (83%), and -1 dB (79%) [Figs. 3(d)–3(f)], with the mode-extinction ratios of ~ 17.5 , 17.3 , and 17.5 dB, respectively. These findings suggest that the designed devices effectively validate the controlled transmission of the interface state based on different modes.

IV. EXPERIMENTAL RESULTS

As a proof of concept, we have successfully fabricated some devices to demonstrate the mode-controlled interface-state switching (see Appendix D for fabrication details). These devices were constructed on a 350 nm silicon-on-insulator (SOI) substrate, with all device parameters matching those used in the simulations. Scanning electron microscope (SEM) images depicting three different design types (corresponding to those in the simulations shown in Fig. 2) are presented in Figs. 4(a)–4(c). To validate the interface-state evolution, an infrared camera in our experiment (see Appendix E) was used to collect the scattered light from the devices. Figure 4(d) depicts the infrared detected images of the normal configuration in Fig. 4(a) under different excited modes (TE and TM). These images clearly show the mode-controlled trace of light along the interface between two topologically nonequivalent networks, coinciding with the simulations in Fig. 2(f). For the L-type deflected-interface [Fig. 4(b)] and the defective-interfaces [Fig. 4(c)] configurations, the traces of light are also mode dependent and localized at interfaces, as shown in Figs. 4(e) and 4(f), respectively.

In addition, we measured the transmission efficiencies of the fabricated devices. The tested wavelengths range from

1540 to 1560 nm, with intervals of 0.4 nm. Experimental efficiency curves for both channels of the normal device are depicted in Figs. 5(a) and 5(d). At specific wavelengths within the gray shaded region, each mode dominates its corresponding channel. For instance, at 1552.52 nm, the measured efficiencies are approximately -5.3 dB (30%) in the TM-interface channel [TM input in Fig. 5(a)] and -5.4 dB (29%) in the TE-interface channel [TE input in Fig. 5(d)], with the mode-extinction ratios of ~ 12.7 and 13.6 dB, respectively. These results quantitatively showcase the successful switching of the interface state controlled by the waveguide mode. In the L-type deflected-interface configuration, the measured efficiencies are approximately -9 dB (12.6%) in the TM-interface channel [Fig. 5(b)] and -10.6 dB (8.7%) in the TE-interface channel [Fig. 5(e)] at 1552.52 nm. The corresponding mode-extinction ratios are ~ 8.3 and 10.5 dB, respectively. These results also demonstrate the switching of the interface state by the input mode, albeit with lower efficiencies than the normal configuration. For the defective-interfaces configuration, the measured efficiencies are approximately -15.6 dB (2.8%) in the TM-interface channel [Fig. 5(c)] and -2.6 dB (55%) in the TE-interface channel [Fig. 5(f)] at a wavelength of 1551.72 nm. The corresponding mode-extinction ratios are ~ 11.3 and 11.2 dB, respectively. The lower measured efficiencies in the TM-interface channel [Fig. 5(c)] than those in the TE channel may be attributed to larger fabrication errors, yet the TM mode remains dominant in this channel.

V. DISCUSSION

In this paper, we experimentally showcase the switching of an anomalous interface state, controlled by the optical-waveguide TE and TM modes with the proposed ROW-based scattering-network system. In this system, the topological

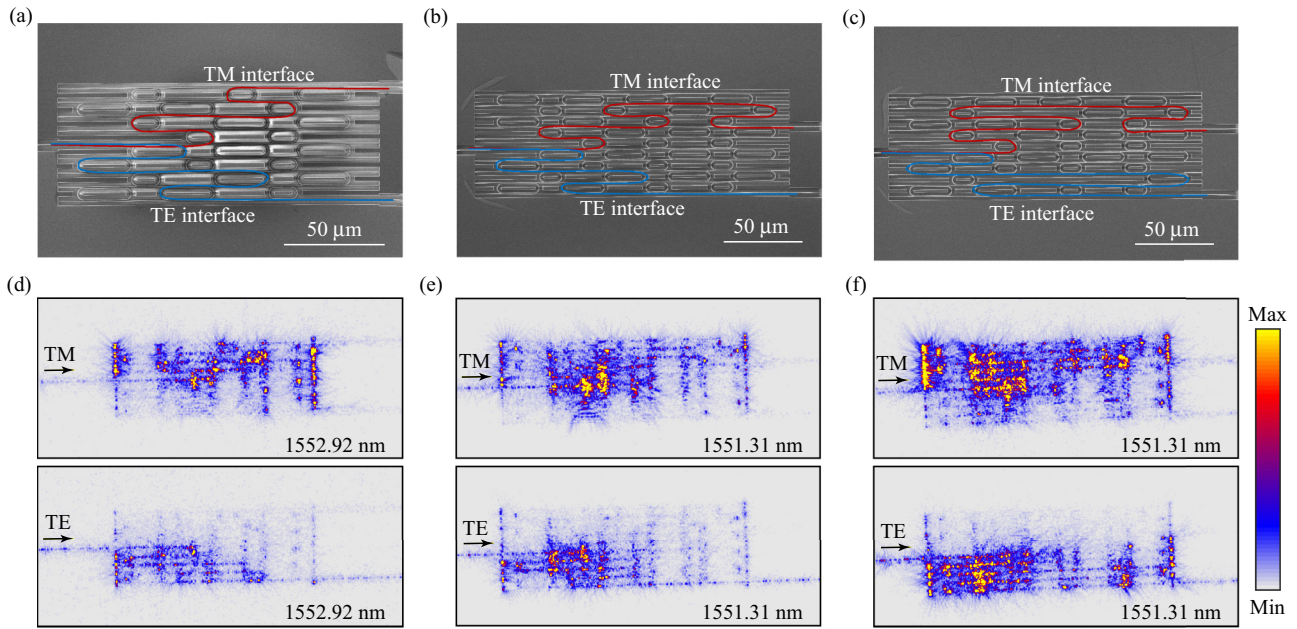


FIG. 4. Experimental results for characterizing the topological interface state. Scanning electron microscopy (SEM) images of the three types of designs: (a) normal, (b) L-type deflected, and (c) defective-interfaces configurations. Near-infrared detected images for (d) normal, (e) L-type deflected, and (f) defective-interfaces configurations. The corresponding excited modes [transverse magnetic (TM) and transverse electric (TE)], and wavelengths (~ 1552 nm) are depicted in each of the subfigures.

invariant (winding number) changes with the mode. Our experimental results demonstrate that the designed devices perform effectively at specific wavelengths, such as those ~ 1552 nm, exhibiting a substantial mode-extinction ratio in

the TE- or TM-interface channel. It is worth noting that the generated interface state in such a ROW-based system is inherently nonchiral, allowing for backward propagation. This characteristic also exists in quantum spin Hall [19,20]

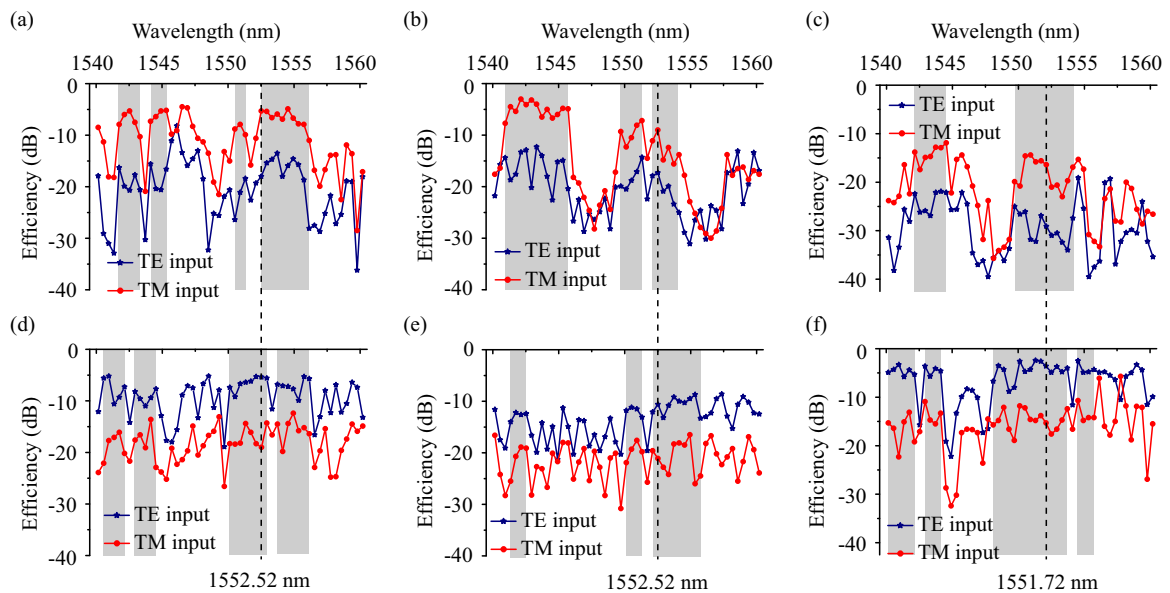


FIG. 5. Experimentally tested efficiency curves for characterizing the topological interface state. The efficiency curves detected in the transverse magnetic (TM) interface channel for the (a) normal, (b) L-type deflected, and (c) defective-interfaces configurations. The gray shaded regions indicate the range of well-working wavelengths. The blue and red curves represent the tested results of transverse electric (TE) and TM modes, respectively. The efficiency curves detected in the TE interface channel for the (d) normal, (e) L-type deflected, and (f) defective-interfaces configurations.

and valley Hall photonic edge modes [33–35]. The underlying mechanism for this phenomenon lies in the reversible scattering process within a single ROW, rooted in the preserved time-reversal symmetry in Maxwell’s equations. To achieve a chiral state, it is necessary to disrupt the time-reversal symmetry through external means like electrical tuning [36]. Nevertheless, the mode-dependent transmission remains unaffected, as the interface-channel trace only slightly deviates from the original when the mode changes, as depicted in Fig. 1(c). Additionally, investigations of utilizing different scattering-network systems (e.g., triangular or kagome lattice [11]) or incorporating additional elements into the waveguide networks may further enrich the manipulation of topological phase. In this paper, we offer an alternative approach to engineer the topological phase, opening possibilities for a range of multifunctional applications in topological photonics.

ACKNOWLEDGMENTS

We thank Pierre Delplace for insightful suggestions and acknowledge the Photonics Center of Shenzhen University and Prof. Shumin Xiao from Harbin Institute of Technology (Shenzhen) for technical support in device fabrication. This paper was supported by the Guangdong Major Project of

Basic and Applied Basic Research No. 2020B0301030009; National Natural Science Foundation of China (Grants No. 61935013, No. 62375181, and No. 61975133); Scientific Instrument Developing Project of Shenzhen University (Grant No. 2023YQ001); Shenzhen Science and Technology Program (Grants No. JCYJ20200109114018750, No. RCJC20231211085920015); Shenzhen Peacock Plan (Grant No. KQTD20170330110444030); and Shenzhen University 2035 Initiative (Grant No. 2023B004).

APPENDIX A: THE SCATTERING-NETWORK MODEL

For the square scattering network in our design, the basic scattering element is a ROW. There are two scattering elements alternatively arranged in the square lattice in Fig. 2(a), the scattering related to the input and output of a single ROW can be described by a scattering matrix:

$$S_\mu = \begin{pmatrix} r_\mu & t_\mu \\ -t_\mu^* & r_\mu^* \end{pmatrix}, \quad (\text{A1})$$

where t_μ is the transmission coefficient and r_μ is the reflection coefficient, $\mu = 1$ or 2 represents the marked number of scattering elements, and the symbol $*$ represents the complex conjugate operation. The relation $|r|^2 + |t|^2 = 1$ is satisfied to preserve the total energy. Assuming the whole process is

lossless, Eq. (A1) can thus be parametrized by

$$S_\mu = \begin{pmatrix} \cos \theta_\mu & i \sin \theta_\mu \\ i \sin \theta_\mu & \cos \theta_\mu \end{pmatrix}, \quad (\text{A2})$$

where the parameter θ_μ controls the transmission and reflection of the scattering process. For the chosen unit cell and the square lattice in Fig. 2(a), the unitary matrix S_μ satisfies

$$\begin{aligned} S_1 \begin{bmatrix} a_1(x, y, t) \\ b_1(x, y, t) \end{bmatrix} &= \begin{bmatrix} a_2(x, y, t + T) \\ b_2(x, y, t + T) \end{bmatrix}, \\ S_2 \begin{bmatrix} a_2(x, y, t) \\ b_2(x - 1, y + 1, t) \end{bmatrix} &= \begin{bmatrix} a_1(x, y + 1, t + T) \\ b_1(x - 1, y, t + T) \end{bmatrix}, \end{aligned} \quad (\text{A3})$$

where T denotes the time needed in the scattering process. When considering the analysis in momentum space and introducing the quasimomentum $\mathbf{k} = (k_x, k_y)$, the Bloch version of the Ho-Chalker operator is [12]

$$S(\theta, \mathbf{k}) = \begin{bmatrix} 0 & S_2(\mathbf{k}) \\ S_1(\mathbf{k}) & 0 \end{bmatrix} = \begin{bmatrix} 0 & 0 & \cos \theta \exp(-ik_y) & i \sin \theta \exp(-ik_x) \\ 0 & 0 & i \sin \theta \exp(ik_x) & \cos \theta \exp(ik_y) \\ \sin \theta & i \cos \theta & 0 & 0 \\ i \cos \theta & \sin \theta & 0 & 0 \end{bmatrix}, \quad (\text{A4})$$

in the state basis $\psi = [a_1(\mathbf{k}), b_1(\mathbf{k}), a_2(\mathbf{k}), b_2(\mathbf{k})]^T$. The eigenvalue phase spectrum of this operator is shown in Fig. 2(b). For the study of edge state, it is convenient to convert the coordinates (x, y) to a nonorthogonal coordinate (x, u) , where u is the direction along the constructed interface, as shown in Fig. 2(c). Hence the Ho-Chalker operator can be rewritten as

$$S(\theta, \mathbf{k}) = \begin{bmatrix} 0 & 0 & \cos \theta \exp[-i(k_x + k_u)] & i \sin \theta \exp(-ik_x) \\ 0 & 0 & i \sin \theta \exp(ik_x) & \cos \theta \exp[i(k_x + k_u)] \\ \sin \theta & i \cos \theta & 0 & 0 \\ i \cos \theta & \sin \theta & 0 & 0 \end{bmatrix}, \quad (\text{A5})$$

by simply substituting k_y with $k_x + k_u$. Eventually, the calculated phase spectrum for Eq. (A5) in the infinite cylinder-geometry network is shown in Fig. 2(d).

APPENDIX B: TOPOLOGICAL PROPERTY OF THE SCATTERING-NETWORK MODEL

In a periodically driven system, considering the unitary evolution $U(t, \mathbf{k})$ with the driven period of T , one can construct an effective Hamiltonian $H_{\text{eff}}(\mathbf{k})$ by the relation:

$$U(T, \mathbf{k}) = \exp[-iT H_{\text{eff}}(\mathbf{k})]. \quad (\text{B1})$$

It shows the effective Hamiltonian can be defined by the logarithm of $U(T, \mathbf{k})$. Assuming $U(T, \mathbf{k})$ is gapped, one can choose the branch cut η of the logarithm in a gap of $U(T, \mathbf{k})$. Then the effective Hamiltonian in this condition can be defined by

$$H_{\text{eff}}^{\eta}(\mathbf{k}) = \frac{i}{T} \ln_{-\eta} U(T, \mathbf{k}), \quad (\text{B2})$$

where the branch cut is chosen by

$$\ln_{-\eta} e^{i\varphi} = i\varphi, \quad -\eta - 2\pi < \varphi < -\eta. \quad (\text{B3})$$

One can further construct a new evolution operator as [12]

$$V_{\eta}(t, \mathbf{k}) = U(t, \mathbf{k}) \exp[it H_{\text{eff}}^{\eta}(\mathbf{k})], \quad (\text{B4})$$

and the winding number can be calculated by

$$W_{\eta}(U) = \frac{1}{24\pi^2} \int_{[0, T] \times \text{BZ}} \text{tr}[(V_{\eta}^{-1} dV_{\eta})^3], \quad (\text{B5})$$

where tr represents the trace operator. When an interface is formed between two periodically driven systems with the evolution operators U_a and U_b . The number of chiral edge states N_{η} in the gap η is thus obtained by

$$N_{\eta} = W_{\eta}(U_a) - W_{\eta}(U_b). \quad (\text{B6})$$

Following the construction in Ref. [12], for the scattering-network construction using the Ho-Chalker operator in this paper, we can interpolate the original Ho-Chalker operator by

$$U_{\text{int}}(S) = \begin{pmatrix} 0 & U_{\text{int}}[S_2] \\ U_{\text{int}}[S_1] & 0 \end{pmatrix}, \quad (\text{B7})$$

where $U_{\text{int}}[S_{\mu}] = \exp(-it H_{\text{eff}}^{-\pi}[S_{\mu}])$ is a new interpolation term that corresponds to the original scattering matrix S_{μ} with a fixed gap at $-\pi$. Then the winding number $W_{\eta}(S)$ for the newly interpolated Ho-Chalker operator in Eq. (B7) can be calculated by Eqs. (B4) and (B5).

APPENDIX C: DESIGN OF ROWs

For achieving the mode-controlled switch of edge state, two scattering elements S_1 and S_2 are set to switchable by the waveguide mode, to simulate the switch of parameter θ_{μ} . Figures 6(a) and 6(b) show the two designed ROW-based scattering elements. One is designed to transmit the TM mode and reflect the TE mode as much as possible [Fig. 6(a)], and the other one is opposite [Fig. 6(b)], corresponding to the scattering elements S_1 and S_2 with switchable parameters θ_1 (θ_2) ≈ 0 and θ_2 (θ_1) $\approx \pi/2$. Such an arrangement is to simulate the switch of parameter θ_{μ} in the scattering network

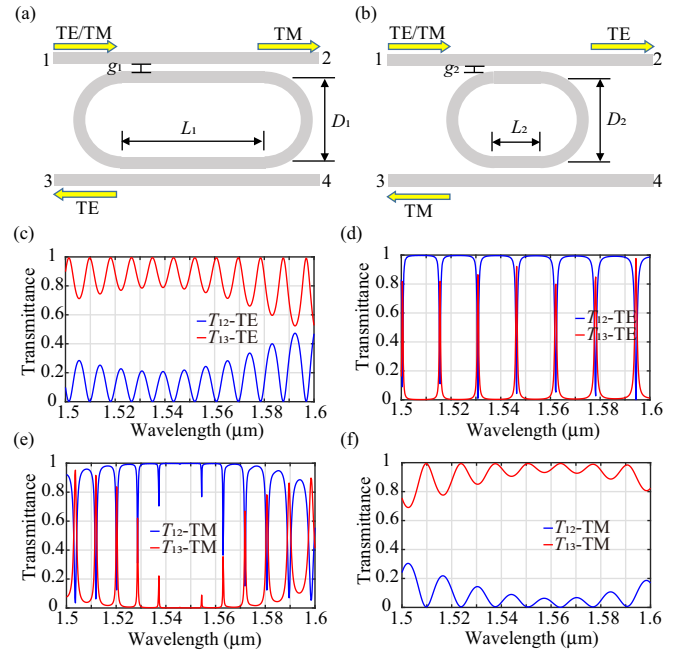


FIG. 6. Mode-controlled ring optical-waveguide (ROW) design. (a) Schematic illustrating the function of the first ROW of transmitting the transverse magnetic (TM) mode and reflecting the transverse electric (TE) mode. The width and height of the waveguide are 420 and 350 nm, respectively. The design parameters include the gap distance (g_1) between the straight and ring waveguides, the length (L_1) of the embedded segments in the ring waveguide, and the diameter (D_1) of the ring waveguide. The specific parameters are $g_1 = 0.1 \mu\text{m}$, $L_1 = 20.5 \mu\text{m}$, and $D_1 = 6 \mu\text{m}$. (b) Schematic depicting the function of the second ROW of transmitting the TE mode and reflecting the TM mode. The corresponding design parameters are $g_2 = 0.16 \mu\text{m}$, $L_2 = 8 \mu\text{m}$, and $D_2 = 5.88 \mu\text{m}$. Simulated transmittance curves for the (c) first ROW and (d) second ROW with the input TE mode. The legends T_{12} and T_{13} represent the transmittance in the through (channel 2) and drop (channel 3) channels, respectively. Simulated transmittance curves for the (e) first ROW and (f) second ROW but with the input TM mode.

by switching the TE and TM modes. The simulation results show the desired functions work well at some wavelengths in the off-resonance region, e.g., $\sim 1550 \text{ nm}$ [Figs. 6(c)–6(f)].

APPENDIX D: DEVICE FABRICATION

The devices were fabricated on a SOI wafer, which consists of a 350-nm-thick device layer and a 2- μm -thick buried oxide layer. The fabrication process involved several steps. Firstly, the SOI sample was spin-coated with a 350-nm-thick layer of ZEP-520A positive resist. It was then baked on a hot plate at 180°C for 3 min. Next, the designed pattern was exposed by the electron beam photolithography using the Raith EBPG 5150. Subsequently, the exposed sample was developed in the n-amyl acetate for 1 min and then fixed in the isopropanol for 30 s at room temperature. Finally, reactive ion etching was employed to remove the undesired silicon layer, with the SiO_2 layer of the wafer severing as the etching stop. The residual resist was wiped off using the N-methyl-2-pyrrolidone. The

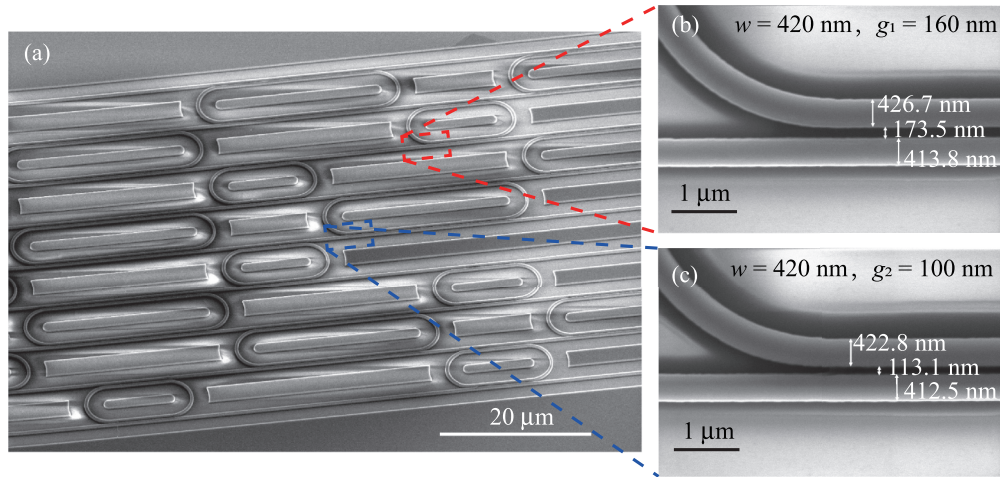


FIG. 7. The scanning electron microscope (SEM) images of the scattering-network waveguides. (a) SEM images for normal configuration. Amplified SEM images for ring optical waveguides with waveguide parameters (b) $w = 420$ nm, $g_1 = 160$ nm and (c) $w = 420$ nm, $g_2 = 100$ nm. The width (gap) errors for the fabricated samples are < 15 nm.

width (gap) errors for the fabricated samples are < 15 nm, as depicted in Fig. 7.

APPENDIX E: EXPERIMENTAL SETUP

In the experimental test, the fabricated device was tested by the infrared detection and the direct measurement of the output power using a coupled lensed fiber. To generate the desired input mode (TE or TM), the state of polarization was modulated in free space using a combination of a polarizer and a half-wave plate. Then the modulated light was coupled to a polarization-maintaining lensed fiber to preserve the polarization states. Finally, the output light from the device was coupled to another lensed fiber and then recorded by a power meter (Fig. 8).

For the infrared-detection part, a near-infrared objective (Mitutoyo, M Plan Apo NIR, 100 \times , numerical aperture = 0.7) and a near-infrared camera (YAMAKO, YM-SC640) were used to collect the light scattered from the devices. The detected images are presented in Fig. 4.

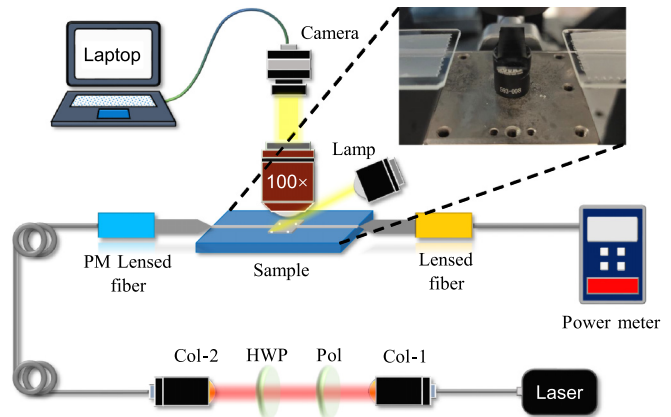


FIG. 8. Experimental setup in the test. PM: polarization maintaining, Col: collimator, HWP: half wave plate, Pol: polarizer.

For the power-measurement part, the measured efficiencies were calibrated with a reference straight waveguide to eliminate the coupling loss of the lensed fiber and the transmission loss in the waveguide, and the results are presented in Fig. 5.

- [1] Y. Hatsugai, *Phys. Rev. Lett.* **71**, 3697 (1993).
- [2] X.-L. Qi, Y.-S. Wu, and S.-C. Zhang, *Phys. Rev. B* **74**, 045125 (2006).
- [3] Y. Hatsugai, *Phys. Rev. B* **48**, 11851 (1993).
- [4] M. Büttiker, *Phys. Rev. B* **38**, 9375 (1988).
- [5] T. Kitagawa, E. Berg, M. Rudner, and E. Demler, *Phys. Rev. B* **82**, 235114 (2010).
- [6] M. S. Rudner, N. H. Lindner, E. Berg, and M. Levin, *Phys. Rev. X* **3**, 031005 (2013).
- [7] L. J. Maczewsky, J. M. Zeuner, S. Nolte, and A. Szameit, *Nat. Commun.* **8**, 13756 (2017).
- [8] S. Mukherjee, A. Spracklen, M. Valiente, E. Andersson, P. Öhberg, N. Goldman, and R. R. Thomson, *Nat. Commun.* **8**, 13918 (2017).
- [9] S. Afzal, T. J. Zimmerling, Y. Ren, D. Perron, and V. Van, *Phys. Rev. Lett.* **124**, 253601 (2020).
- [10] F. Gao, Z. Gao, X. Shi, Z. Yang, X. Lin, H. Xu, J. D. Joannopoulos, M. Soljačić, H. Chen, L. Lu *et al.*, *Nat. Commun.* **7**, 11619 (2016).
- [11] P. Delplace, *SciPost Physics* **8**, 081 (2020).
- [12] P. Delplace, M. Fruchart, and C. Tauber, *Phys. Rev. B* **95**, 205413 (2017).
- [13] M. Bellec, C. Michel, H. Zhang, S. Tzortzakis, and P. Delplace, *EPL* **119**, 14003 (2017).
- [14] J. T. Chalker and P. D. Coddington, *J. Phys. C Solid State Phys.* **21**, 2665 (1988).
- [15] Z. Zhang, P. Delplace, and R. Fleury, *Nature (London)* **598**, 293 (2021).

- [16] Z. Zhang, P. Delplace, and R. Fleury, *Sci. Adv.* **9**, eadg3186 (2023).
- [17] L. Lu, J. D. Joannopoulos, and M. Soljačić, *Nat. Photonics* **8**, 821 (2014).
- [18] T. Ozawa, H. M. Price, A. Amo, N. Goldman, M. Hafezi, L. Lu, M. C. Rechtsman, D. Schuster, J. Simon, O. Zilberberg *et al.*, *Rev. Mod. Phys.* **91**, 015006 (2019).
- [19] M. Hafezi, E. A. Demler, M. D. Lukin, and J. M. Taylor, *Nat. Phys.* **7**, 907 (2011).
- [20] M. Hafezi, S. Mittal, J. Fan, A. Migdall, and J. M. Taylor, *Nat. Photonics* **7**, 1001 (2013).
- [21] S. Mittal, V. V. Orre, D. Leykam, Y. D. Chong, and M. Hafezi, *Phys. Rev. Lett.* **123**, 043201 (2019).
- [22] S. Afzal, T. J. Zimmerling, and V. Van, in *Silicon Photonics IV*, edited by D. J. Lockwood and L. Pavesi, Topics in Applied Physics (Springer, Cham, 2021), Vol. 139, p. 365.
- [23] G. Q. Liang and Y. D. Chong, *Phys. Rev. Lett.* **110**, 203904 (2013).
- [24] M. Pasek and Y. D. Chong, *Phys. Rev. B* **89**, 075113 (2014).
- [25] S. Afzal and V. Van, *Opt. Express* **26**, 14567 (2018).
- [26] T. Dai, Y. Ao, J. Bao, J. Mao, Y. Chi, Z. Fu, Y. You, X. Chen, C. Zhai, B. Tang *et al.*, *Nat. Photonics* **16**, 248 (2022).
- [27] K. E. Arledge, B. Uchoa, Y. Zou, and B. Weng, *Phys. Rev. Res.* **3**, 033106 (2021).
- [28] A. Nagulu, X. Ni, A. Kord, M. Tymchenko, S. Garikapati, A. Alù, and H. Krishnaswamy, *Nat. Electron.* **5**, 300 (2022).
- [29] L. He, Z. Addison, J. Jin, E. J. Mele, S. G. Johnson, and B. Zhen, *Nat. Commun.* **10**, 4194 (2019).
- [30] J. Jin, L. He, J. Lu, L. Chang, C. Shang, J. E. Bowers, E. J. Mele, and B. Zhen, [arXiv:2304.09385](https://arxiv.org/abs/2304.09385).
- [31] C. M. Ho and J. T. Chalker, *Phys. Rev. B* **54**, 8708 (1996).
- [32] A. C. Potter, J. T. Chalker, and V. Gurarie, *Phys. Rev. Lett.* **125**, 086601 (2020).
- [33] T. Ma and G. Shvets, *New J. Phys.* **18**, 025012 (2016).
- [34] M. I. Shalaev, W. Walasik, A. Tsukernik, Y. Xu, and N. M. Litchinitser, *Nat. Nanotechnol.* **14**, 31 (2019).
- [35] C. A. Rosiek, G. Arregui, A. Vladimirova, M. Albrechtsen, B. Vosoughi Lahijani, R. E. Christiansen, and S. Stobbe, *Nat. Photonics* **17**, 386 (2023).
- [36] O. E. Örsel, J. Noh, and G. Bahl, *Nanophotonics* **13**, 173 (2024).